RSC Advances

PAPER

View Article Online
View Journal | View Issue

Check for updates

Cite this: *RSC Adv.*, 2018, **8**, 12420

Photoreduction route for Cu_2O/TiO_2 nanotubes junction for enhanced photocatalytic activity†

Van Viet Pham, *[a] Dai Phat Bui, [a] Hong Huy Tran, [a] Minh Thi Cao,[b] Tri Khoa Nguyen,[c] Yong Soo Kim *[c] and Van Hieu Le[a]

Received 12th February 2018
Accepted 23rd March 2018

DOI: 10.1039/c8ra01363b

rsc.li/rsc-advances

Here, we synthesized copper(I) oxide and titanium dioxide nanotubes (TNTs) heterojunctions (HJs) by a photoreduction method using a low-power UV lamp without involving any additional steps, such as chemical reduction, surfactant, or protection agents. Transmission electron microscopy, X-ray diffraction, Raman scattering, X-ray photoelectron spectroscopy, diffuse reflectance spectra, and photoluminescence spectroscopy were carried out to verify the formation of a HJ between the Cu_2O nanoparticles (Cu_2O NPs) and TNTs. The efficiency and the rate of methylene blue photo-degradation over the Cu_2O/TNTs HJ were found to be nearly double and triple compared to the isolated TNTs. The enhanced efficiency is attributed to the narrow band gap and defect states caused by the oxygen vacancies in the vicinity of HJs. Moreover, the type II band alignment of Cu_2O NPs and TNTs naturally separates the photo-generated carriers and constrains the recombination process owing to the internal electric field across the Cu_2O/TNTs interface.

Open Access Article. Published on 03 April 2018. Downloaded on 5/3/2026 11:28:47 AM.
This article is licensed under a Creative Commons Attribution-NonCommercial 3.0 Unported Licence.

Introduction

Titanium dioxide nanotubes (TNTs) have attracted tremendous scientific and technological interest owing to their peculiar properties for diverse applications.[1] However, the photocatalytic efficiency of pure TNTs is low because of their wide band gap and fast recombination of photo-generated electron and hole pairs.[1,2] In order to achieve these desired performances, the formation of homojunctions and heterojunctions of TNTs is preferred.[3–5] Recently, heterojunctions (HJs) among n-type TNTs and various narrow band gap p-type semiconducting materials with a well aligned band structure is proven to be an effective way of overcoming the drawbacks of TNTs.[6–10] This combination also provides a strong driving force for charge carrier separation owing to the strong internal electric field.[7,8] Among various p-type semiconducting materials, cuprous oxide (Cu_2O) possesses a direct energy gap ($E_g \approx 2.17$ eV). The conduction band (CB) and valence band (VB) of Cu_2O lie higher than those of TiO_2, which is favorable for the efficient separation of photogenerated charge carriers. Moreover, Cu_2O is abundant as well as nontoxic in nature, which render it for the photocatalytic activity of TNTs.[9,11–17] The idea have motivated many research groups to investigate the photocatalytic activity of loaded Cu_2O nanoparticles (NPs) on the surface of TiO_2 nanotube array (TNA) synthesized from titanium foils *via* anodization method.[6,12,18–20] Although the direct deposition of Cu_2O NPs on TNA is comparatively easier owing to their self-organized orientation, however, Cu_2O NPs should be loaded on above the side or on the internal walls of the TNA to enhance its photocatalytic activity.[12] Furthermore, the synthesis of TNAs depends on many synthetic parameters (anodizing voltage, reaction time, electrolyte, annealing temperature, *etc.*) and so far it has been only prepared on titanium surface having a small area, which limits its industrial scale applications.[21–23] Meanwhile, there are limited reports available on the direct loading of Cu_2O NPs over the entire surface of hydrothermally synthesized-TNTs, which have a high specific surface area.[13]

Cu_2O NPs can be loaded onto TNTs *via* several approaches. Photoreduction method is one of the low cost as well as high reaction efficiency method that can be applied to practical applications.[24,25] Recently, the photoreduction approach was applied to fabricate Cu_2O/TiO_2 composite.[12,18,26–28] For instance, the TNA has been synthesized by anodization Ti foil and the photoreduction approach was applied to load Cu_2O NPs over TNA using aqueous Cu^{2+} ions and by exposing it to a 300 W UV lamp under slightly acidic conditions.[12,18] Also, TiO_2 nanosheets have been synthesized *via* hydrothermal method. After mixing these sheets with an aqueous Cu^{2+} solution in a vacuum pumped quartz conical flask under UV irradiation in argon environment results in Cu_2O/TiO_2 composite.[27]

Here, we present the direct loading of Cu_2O NPs on hydrothermally synthesized TNTs *via* a photoreduction method using

[a]*Nanomaterials for Environmental Applications Laboratory, Faculty of Materials Science and Technology, University of Science, VNU-HCMC, Ho Chi Minh City 700000, Vietnam. E-mail: pvviet@hcmus.edu.vn*

[b]*CM Thi Laboratory, Ho Chi Minh City University of Technology (HUTECH), Ho Chi Minh City 700000, Vietnam*

[c]*Department of Physics and Energy Harvest-Storage Research Center, University of Ulsan, Ulsan 44610, South Korea. E-mail: yskim2@ulsan.ac.kr*

† Electronic supplementary information (ESI) available. See DOI: 10.1039/c8ra01363b

This journal is © The Royal Society of Chemistry 2018

Open Access Article. Published on 03 April 2018. Downloaded on 5/3/2026 11:28:47 AM.
This article is licensed under a Creative Commons Attribution-NonCommercial 3.0 Unported Licence.

a low-power UV lamp (low-pressure mercury lamp; $\lambda = 254$ nm, 18 W) to form Cu_2O/TNTs junction. This process does not involve any additional assistant or chemical reducing agent. The experiments were conducted at ambient conditions and free of pH adjustment with alkali or acid. In addition, we thoroughly discuss the root of the narrowed band gap, broaden absorption region, and enhanced photo-degradation of Cu_2O/TNTs. Moreover, the formation of HJ and its photocatalytic mechanisms are also investigated.

Experiment

Chemicals and materials

Commercial TiO_2 powder (Merck, 99.99%), sodium hydroxide (NaOH, Merck, 99%), hydrochloric acid at a 37% concentration (HCl, Merck, 99.99%), acetone (C_3H_6O, ChemSol, 99%), ethanol (C_2H_6O, ChemSol, 99%), $Cu(NO_3)_2$ (Xilong Chemical Co., 99%), methylene blue (MB, JHD Fine Chemicals, 99%), and deionized (DI) water (Puris-Evo water system) were used as received.

Preparation of TNTs by hydrothermal method

The TNTs were prepared by the hydrothermal method reported elsewhere.[29] Initially, 1.7 g of TiO_2 powder was dissolved in 157 mL of 10 M NaOH. The mixture was then transferred to a stainless autoclave and heated to 135 °C for 24 h. The resulting product was treated with HCl and later washed with deionized water (DI) until an unchanged pH value was achieved. Finally, the product was dried at 100 °C for 5 h.

The preparation of Cu_2O/TNTs

The Cu_2O/TNTs synthesis procedure is summarized as follows; a 7.53 g of TNT powder was dispersed in 125 mL of 0.02 M $Cu(NO_3)_2$ for 45 min. The pH of the mixture was found to be 5 using a portable pH meter (Hanna, Romania). The mixture was then magnetically stirred continuously and exposed to UV light (low-pressure mercury lamp, 18 W, $\lambda = 254$ nm) for 24 h. The pH at this step was approximately 6. Subsequently, the product was washed repeatedly with DI water and dried at 100 °C for 5 h.

Material characterization

The phase, chemical composition, and crystal structure of Cu_2O/TNTs were examined by X-ray diffraction (XRD; Bruker, D8-Advance 5005) using Cu Kα radiation ($\lambda = 0.154064$ nm) and Raman scattering spectroscopy (Jobin Yvon – Labram 300 spectrometer, excitation source; He–Ar laser with $\lambda = 514.5$ nm). The morphology of the samples was examined by transmission electron microscopy (TEM; JEOL, JEM 1400). Energy dispersive X-ray spectroscopy (EDS; JEOL, JSM-7401F) was used to determine the weight and atomic percentage of the elements. The chemical states of copper, titanium, and oxygen in the materials were analyzed by X-ray photoelectron spectroscopy (XPS; Leybold, ESCALAB250, Theta Probe XPS system) using an Al Kα monochromatic beam (1486.6 eV). The optical characterization was analyzed by diffuse reflectance spectroscopy (DRS) over the wavelength range of 200–800 nm using an UV-Vis spectrometer (JASCO-V550). Photoluminescence (PL; Horiba Jobin-Yvon Nanolog) analysis with 325 nm excitation source (Xe lamp) was performed at the room temperature to examine the optical and photochemical properties.

Evaluation of the photocatalytic activity

The photocatalytic activity of the materials was evaluated by measuring the level of methylene blue (MB) photodegradation under simulated sunlight irradiation. Initially, 60 mL of MB solution with an initial concentration of 6.25×10^{-5} (mol L^{-1}) and 0.02 g of catalyst were stirred magnetically for 60 min to reach the adsorption/desorption equilibrium in the dark. The mixture was then irradiated with a simulated Xenon lamp (ABET 230 V, 150 W, 300 nm $\leq \lambda \leq$ 1800 nm) for 150 min. The absorption spectra of MB were recorded at regular intervals (30 min) of irradiation. The experiments to determine the photocatalytic activity were repeated three times. The photocatalytic efficiency was determined using the following formula, $\eta[\%] = (C_0 - C_t)/C_0 \times 100$, where η is the degradation efficiency, C_0 is the absorption intensity of the MB solution after the adsorption/desorption reached the equilibrium, and C_t is the absorption intensity of the MB solution at time t.

Reaction kinetic model

The Langmuir–Hinshelwood model has been used to determine the reaction rate constant for the photocatalytic reaction in gas-phase or in liquid-phase.[30] To fit the experimental data, the adsorption can be reduced and the following linear form of Langmuir–Hinshelwood equation (eqn (1)) for the first-order reaction is used[31]

$$\ln\left(\frac{C}{C_0}\right) = -kt \quad (1)$$

where C represents the concentration in solution of MB being degraded (mg L^{-1}), C_0 is the initial concentration of MB, k is apparent reaction rate constant of ideal first order equation (min^{-1}) and t is photocatalytic reaction time (min).

Results and discussion

Crystallinity and morphology

Fig. 1a shows the X-ray diffraction (XRD) patterns of the TNTs (black) and Cu_2O/TNTs (red). The observed XRD peaks of TNTs at $2\theta = 25.34°$, 37.79°, 48.08°, 55.01°, 62.78°, 68.84°, 70.37°, and 75.11°, corresponding to the (101), (004), (200), (211), (204), (116), (220), and (301) planes, respectively, of the anatase phase of TiO_2 (JCPDS no. 21-1272). In addition, other peaks at $2\theta =$ 27.50°, 36.08°, 41.30°, and 54.35° were assigned to the (110), (101), (111), and (211) planes, respectively, of the rutile phase of TiO_2 (JCPDS no. 21-1276). The XRD pattern of the Cu_2O/TNTs reveals the existence of an additional XRD peak at 29.12°, corresponding to the (110) plane of Cu_2O (JCPDS no. 05-0667). Furthermore, the decreasing intensity of the crystal peak of the TNTs can be attributed to the coverage of Cu_2O NPs on the TNT surface or be caused by the soak in water and the effect of UV light during the photoreduction process.[32]

Open Access Article. Published on 03 April 2018. Downloaded on 5/3/2026 11:28:47 AM.
This article is licensed under a Creative Commons Attribution-NonCommercial 3.0 Unported Licence.

Raman scattering was used to further elaborate the phases and individual components in the Cu_2O/TNTs composite. The spectrum was taken in 100–1000 cm^{-1} range. Raman spectrum (Fig. 1b) of isolated TNTs (black) shows six active modes of the anatase phase *i.e.* E_g (142, 195, and 639 cm^{-1}), B_{1g} (399 cm^{-1}) and $A_{1g} + B_{1g}$ (513 cm^{-1}). Moreover, it also shows two peaks E_g (447 cm^{-1}) and B_{2g} (826 cm^{-1}) corresponding to the rutile phase of TNTs.[33–35] The Raman spectrum (red) of the Cu_2O/TNTs in the rutile phase revealed a peak at 447 cm^{-1} (E_g) with higher intensity and an additional peak at 826 cm^{-1} (B_{2g}). The peak at 110 cm^{-1} corresponds Cu_2O in the composite.[36] In addition, the peak at 265 cm^{-1} can be attributed to the Ti–OH bonds in the TNT tubular structure. The comparatively higher intensity of this peak could be caused by the water absorption by the Ti–O bonds during the photoreduction process.[37] The Raman results further confirm the existence of Cu_2O in the product.

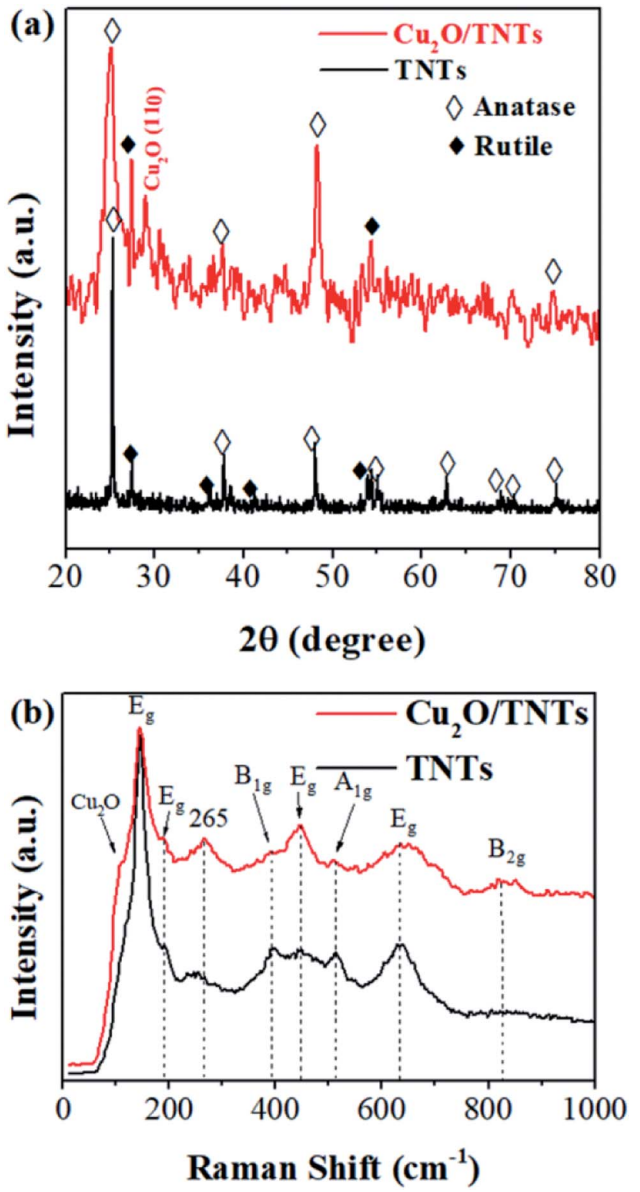

Fig. 1 (a) XRD patterns and (b) Raman spectra of TNTs and Cu_2O/TNTs.

Fig. 2 shows TEM images of the TNTs and Cu_2O/TNTs at different magnifications. The morphology of the TNTs shows typical tubular structure consists of uniform nanotubes (Fig. 2a and c). The outer and inner diameter were found to 8 ± 2 nm and 4 ± 2 nm, respectively. The lengths of TNTs ranged from 200 to 400 nm. Fig. 2b and d exhibit the TEM images of the Cu_2O/TNTs, spherical Cu_2O NPs (diameter: 6–8 nm) over TNTs, as also confirmed by XRD and Raman results. The Cu_2O NPs are evenly showing rather a rough surface owing to the accumulation of small particles distributed over the entire surface of TNTs, which have high specific surface area providing a large number of active sites. Moreover, the tubular morphology of the TNTs is still preserved, as evident in the Fig. 2b and d, respectively. This observation shows that the loading of Cu_2O NPs does not induce any change in the TNT morphology after the photoreduction process. Therefore, the Cu_2O NPs have been successfully loaded on the TNT surface and the HJ is formed. The chemical composition was analyzed by EDS, as shown in Fig. 2f. The energy dispersive X-ray spectroscopy (EDS) results revealed the presence of Ti, O, and Cu with atomic percentages of 19.67%, 60.46%, and 0.95%, respectively.

The elemental oxidation states were investigated by high-resolution XPS (HR-XPS). Fig. 3a reveals two peaks at 464.3 eV and 458.6 eV corresponding to the Ti $2p_{1/2}$ and Ti $2p_{3/2}$ of Ti^{4+}

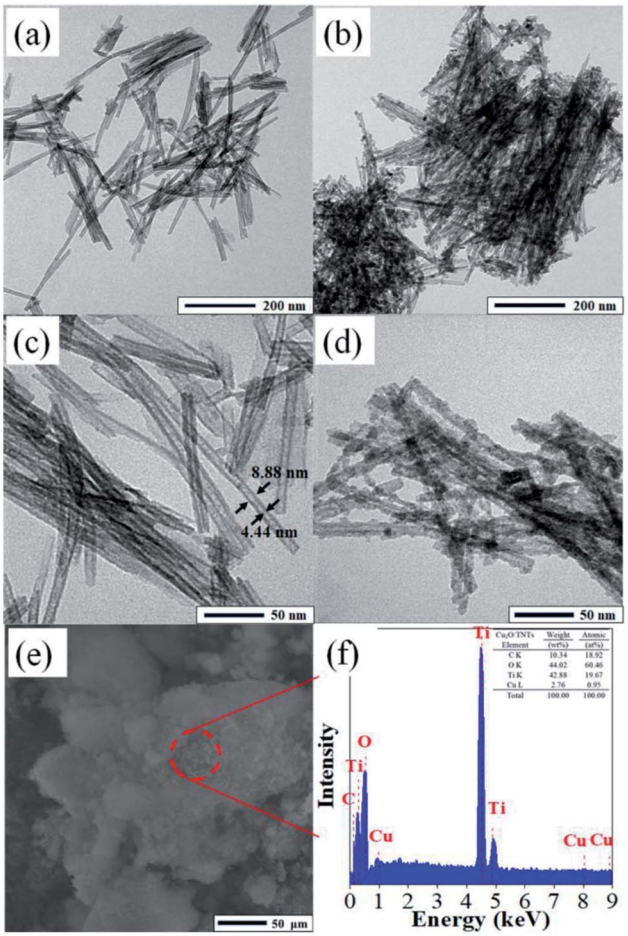

Fig. 2 TEM images of TNTs (a and c) and Cu_2O/TNTs (b and d); (e and f) SEM image and EDS pattern of Cu_2O/TNTs.

This journal is © The Royal Society of Chemistry 2018

Open Access Article. Published on 03 April 2018. Downloaded on 5/3/2026 11:28:47 AM.
This article is licensed under a Creative Commons Attribution-NonCommercial 3.0 Unported Licence.

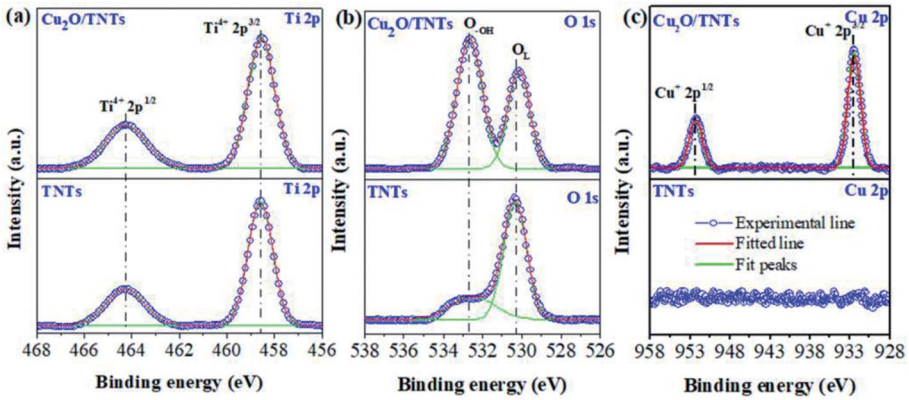

Fig. 3 High-resolution XPS analysis of Ti 2p (a), O 1s (b), and Cu 2p (c) of TNTs and Cu_2O/TNTs.

states in TiO_2, respectively.[38] Moreover, the percentage of Ti $2p_{1/2}$ and Ti $2p_{3/2}$ of Ti^{4+} states in the TNTs are found to be 31.3% and 68.7%, respectively. No significant change in these states was observed in the Cu_2O/TNTs (see Table 1) indicating that the loading of Cu_2O NPs onto TNTs does not affect the Ti 2p oxidation states of the TNTs. The peaks correspond to O 1s states of O^{2-} species in the lattice (O_L), surface hydroxyl oxygen (O_{-OH}) in TNTs was found to be at 530.3 eV and 532.5 eV, respectively (Fig. 3b).[39] Moreover, after loading Cu_2O NPs, the binding energy of lattice oxygen slightly shifts from 530.3 eV to 530.1 eV and also increase of surface hydroxyl oxygen, indicating the formation of oxygen vacancies (V_O), as shown in Table S1†.[40] In particular, Table 2 shows that the percentage of O_L decreases and that of O_{-OH} increases when Cu_2O NPs loaded onto the TNT surface. Aforementioned, the increase of O_{-OH} is derived from photoreduction process as has been confirmed by the increase of the Ti–OH peak at 265 cm^{-1} in Raman analysis. The increase of O_{-OH} indicates the formation of V_O leading to the higher photocatalytic performance.[39,40] Furthermore, Fig. 3c shows Cu 2p XPS spectrum of Cu_2O/TNTs with Cu $2p_{1/2}$ and $2p_{3/2}$ lines at the binding energy of about 932.5 eV and 952.5 eV, respectively, which demonstrates the existence of Cu_2O on the surface of TNTs.[38]

The formation of Cu_2O NPs during the photoreduction process can be explained as follows: when the TNTs are excited by UV light, electrons from the valance band (VB) transfer to the conduction band (CB) and form an electron–hole (e–h) pairs. It is well known that Cu^{2+} can be photoreduced if Cu^{2+} couple possesses a redox potential more positive than the flat band potential of the CB. The reductions of Cu^{2+} as following (eqn (2)–(4)).

$$Cu^{2+} + e \rightarrow Cu^{+},\ E^0_{Cu^{2+}/Cu^{+}} = 0.153\ V \quad (2)$$

$$Cu^{2+} + 2e \rightarrow Cu,\ E^0_{Cu^{2+}/Cu} = -1.25\ V \quad (3)$$

$$Cu^{+} + e \rightarrow Cu,\ E^0_{Cu^{+}/Cu} = -2.53\ V \quad (4)$$

Therefore, the formation of Cu_2O NPs on TNTs can be interpreted as follows; $E^0_{Cu^{2+}/Cu^{+}} = 0.153$ V is more positive than the flat band potential of the CB that is about −0.56 V, and therefore, Cu^{2+} can be photoreduced to Cu^{+}. The redox potentials of two other copper couples are more negative than the flat band potential of the CB, so Cu^{2+} cannot be photoreduced to Cu, and Cu^{+} cannot be photoreduced to Cu.[41,42] The stability of Cu_2O is shown in Fig. S2–4.†

Optical characterization

Fig. 4 shows the DRS results of the TNTs (black) and Cu_2O/TNTs (red), respectively. The energy band structure of TNTs suggests strong optical absorption at the short wavelength range compared to long wavelength. The absorption edge at 402 nm is attributed mainly to the electron transitions from the VB to CB (band-to-band transition, O 2p → Ti 3d orbital). In contrast, the Cu_2O/TNTs shows three absorption features. The absorption edge corresponds to an interband transition significantly red shifts to 441 nm. The absorption at wavelengths than 650 nm is consistent with the intraband absorption of Cu_2O NPs.[43]

The increase in optical absorption observed in the 700–800 nm range can be understood in terms of d–d transition of copper ions.[44–47] It does not enhance the number of

Table 1 Ti content and binding energy of Ti 2p state for TNTs and Cu_2O/TNTs samples

	Ti^{4+} $2p_{1/2}$		Ti^{4+} $2p_{3/2}$	
Sample	BE (eV)	Ti content (%)	BE (eV)	Ti content (%)
TNTs	464.3	31.3	458.6	68.7
Cu_2O/TNTs	464.3	33.9	458.6	66.1

Table 2 O content and binding energy of Ti 2p state for TNTs and Cu_2O/TNTs samples

	Ti–OH		TiO_2	
Sample	BE (eV)	O content (%)	BE (eV)	O content (%)
TNTs	532.5	48.8	530.3	51.2
Cu_2O/TNTs	532.6	60.9	530.1	39.1

Open Access Article. Published on 03 April 2018. Downloaded on 5/3/2026 11:28:47 AM.
This article is licensed under a Creative Commons Attribution-NonCommercial 3.0 Unported Licence.

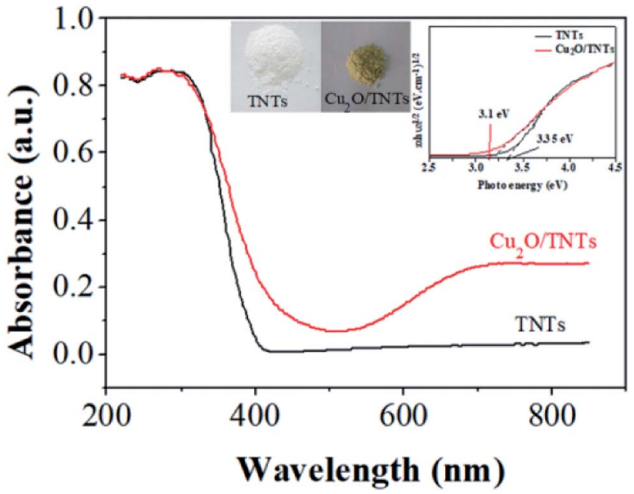

Fig. 4 UV-Vis diffuse reflectance spectra of the TNTs and Cu_2O/TNTs.

photogenerated carriers but rather increase the carrier lifetime.[48] Clearly, the appearance of an optical absorption shoulder in the visible region leads to two-phase absorption *i.e.* UV and visible. Additionally, the inserted digital photographs (Fig. S3†) of the TNTs and Cu_2O/TNTs samples show that after the photoreduction process, the color of the resulting powder changes from white for TNTs to light yellow for Cu_2O/TNTs. The observation shows a striking contrast to the white color of pure TNTs. This result indicates that the photoreduction process affected the surface properties of TNTs. As a result, this change of the color could be induced an enhanced photo-absorption.

The band gap energy of the materials can be approximated using the following equation:

$$\alpha h\nu = A(h\nu - E_g)^2 \quad (5)$$

where α, ν, A and E_g are absorption coefficient, Plank's constant, light frequency, a constant, and band gap energy, respectively.[49]

It is clear from eqn (5) that the band gap E_g can be obtained by extrapolating to zero a linear fit to a plot of $(\alpha h\nu)^2$ against $h\nu$ (often referred to as a Tauc plot). The estimated optical band gaps of the TNTs and Cu_2O/TNTs were found to be 3.35 eV and 3.1 eV, respectively. The extended photoactive wavelength up to 441 nm is the result of the band gap reduction of the Cu_2O/TNTs HJ caused by hybridization of the O 2p and Ti 3d orbital and/or also the presence of the mid-gap energy states (defect states).[50–52] The DRS result of Cu_2O/TNTs show this reduction of TNTs band edge structure and the presence of Cu_2O NPs allowing intraband transition, which induces a higher lifetime of photogenerated carriers, as well as extending of the HJ absorption region.

The PL spectrum acquired from TNTs shows three emission peaks at 438 nm (2.83 eV), 532 nm (2.33 eV), and 632 nm (1.96 eV) respectively, as depicted in bottom part of Fig. 5a. These peaks can be attributed to the excitonic transitions from TiO_2 intrinsic defects as the self-trapped exciton (STE) and surface defect states including oxygen vacancies ($V_{O,S}$), O^- vacancies ($V_O^{\cdot}$), as schematically shown in Fig. 5b.[53–55] Therein, the STE is caused by the interaction of electrons in the CB localized on the Ti_{3d} orbital with holes in the O_{2p} orbital of TNTs.[56] The existence of ($V_O^{\cdot}$) defects can be explained in terms of holes in the VB reacting with O^{2-} in the TNT structure to produce $^{\cdot}O^-$ (eqn (6)), which then immediately react with each other to release O_2 on the surface (eqn (7)).[57] The peak located at ~1.96 eV corresponding to the range of wavelength in the visible light region is suggested to be $V_{O,S}$ defects.[58] The presence of these defects was derived by reactions in the hydrothermal environment, which is well known to cause defects in the material structure. The percentages of the PL peaks at 2.83 eV, 2.33 eV, and 1.96 eV were 26.84%, 42.01%, and 31.15% (see Table 3), respectively.

$$h\nu_{VB}^{+} + O^{2-} \rightarrow {}^{\cdot}O^- \quad (6)$$

$$2{}^{\cdot}O^- \rightarrow O_2 \quad (7)$$

The PL spectrum from Cu_2O/TNTs (up part of Fig. 5a) is the superposition of three similar emissions at 446 nm (2.79 eV), 529 nm (2.34 eV), and 629 nm (1.97 eV), respectively. However,

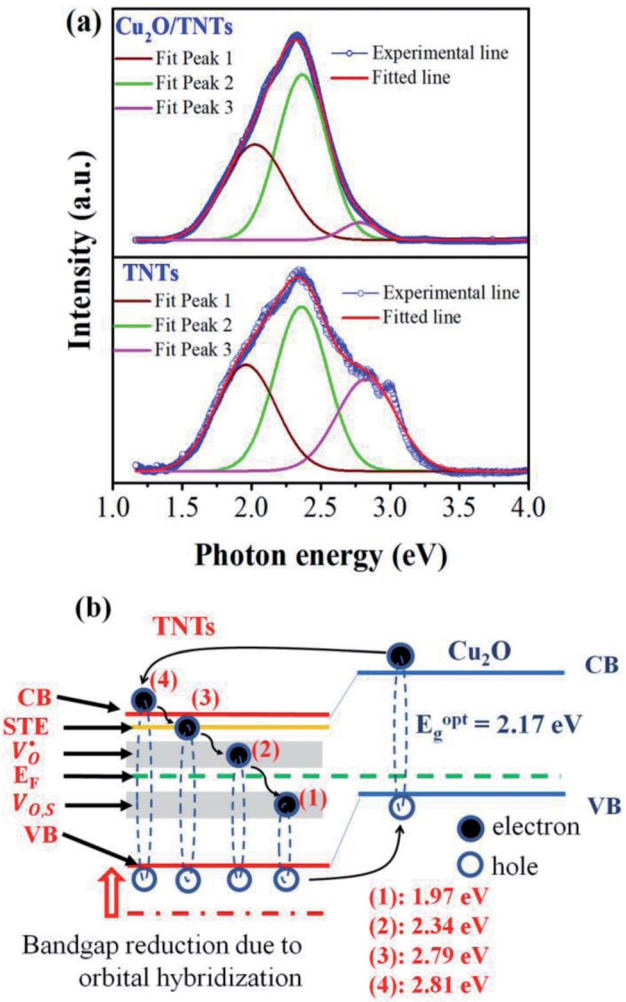

Fig. 5 Photoluminescence spectra of the TNTs and Cu_2O/TNTs (a); schematic illustration of the change of the band gap of heterojunction structure of Cu_2O/TNTs (b).

This journal is © The Royal Society of Chemistry 2018

Open Access Article. Published on 03 April 2018. Downloaded on 5/3/2026 11:28:47 AM.
This article is licensed under a Creative Commons Attribution-NonCommercial 3.0 Unported Licence.

Table 3 Energy and relative portion of the electron–hole recombination transitions in the TNTs and Cu_2O/TNTs samples

TNTs			Cu_2O/TNTs		
Position	Area	%	Position	Area	%
2.83	886.91	26.84	2.79	645.49	4.13
2.36	1388.14	42.01	2.37	8716.06	55.77
1.96	1029.11	31.15	1.97	6267.51	40.10

the peak arising at 1.97 eV, corresponds to $V_{O,S}$ defects, is substantially higher than that of the TNTs after loading Cu_2O NPs. The increase of $V_{O,S}$ defects provides trap sites for charge carriers and contributes to the reduction of the band gap, as be shown in DRS result.[51] Moreover, the radiative combination of the e–h pair in STE is not favorable, leading to the relatively high photocatalytic activity of TNTs.[59]

Photocatalytic activity of TNTs and Cu_2O/TNTs

The photocatalytic activity of the TNTs and Cu_2O/TNTs were evaluated through the methylene blue (MB) degradation ability for 150 min under sunlight, as shown in Fig. 6a. It shows that the photodegradation of MB on the Cu_2O/TNTs is very fast for the initial 30 min and then gradually decreases, and almost completely decomposes the MB after 150 min of the sunlight irradiation. The MB photodegradation efficiency of Cu_2O/TNTs is nearly double compared to isolated TNTs after 150 min of exposure (81.70% and 43.73% for Cu_2O/TNTs and TNTs, respectively). Moreover, the phenol photodegradation by materials was observed to confirm the photocatalytic performance of materials with non-color pollutant (Fig. S1†). For a quantitative comparison, we used the Langmuir–Hinshelwood model to describe the rates of the MB photodegradation over the materials. Notably, the initial MB photodegradation was recognized to follow mass transfer controlled first-order kinetics comparatively as a result of low-concentration target pollutants, as evidenced by the linear plot of $\ln(C/C_0)$ *versus* photocatalytic reaction time t. Fig. 6b shows that the initial rate constant of MB degradation over Cu_2O/TNTs for the first 30 min under sunlight irradiation was estimated as 0.0329 min^{-1}, which was three times faster than that over TNTs (0.0128 min^{-1}). Fig. 6c and d exhibit that the absorption spectrum of MB negligibly changed after 150 min under sunlight irradiation, while the absorption spectrum of MB over Cu_2O/TNTs drastically changed, particularly, the typical absorption peak of MB at 664 nm strongly decreased after 150 min. These results confirmed that the abasement of MB absorption peak intensity was caused by the photodegradation of catalyst not by photolysis of MB. These observations indicate that the HJ formation significantly affected the photocatalytic activity of the material because of its influences on the photocatalyst microstructure and band structure as evidenced by XRD, TEM, XPS, DRS, and PL characterizations.

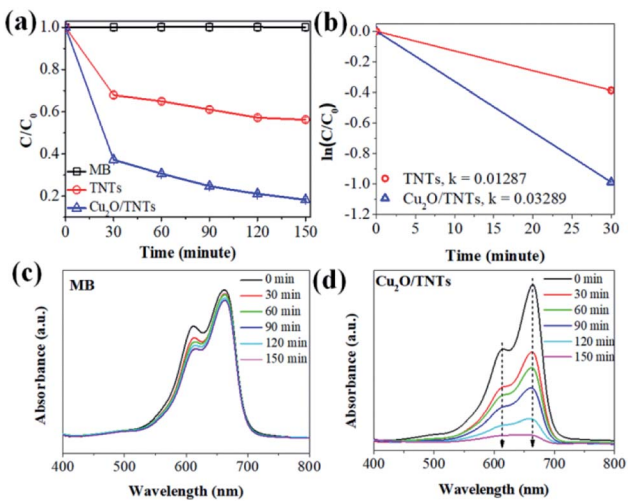

Fig. 6 (a) Photocatalytic activity of the TNTs and Cu_2O/TNTs under sunlight irradiation, (b) plots of the dependence of concentration on irradiation time for the first 30 m, (c and d) the absorption spectra of MB and MB over Cu_2O/TNTs for 150 minutes under sunlight irradiation.

Fig. 7 schematically explain the mechanism of photocatalysis of Cu_2O/TNTs p–n junction under sunlight irradiation. When a visible light ray interacts with Cu_2O/TNTs, it excites the narrow gap Cu_2O NPs and generates e–h pairs in respective CB and VB, respectively (eqn (8)). The photo-induced electrons in the CB of p-type Cu_2O NPs easily transfer to n-type TNTs due to the energy gradient owing to the type-II band alignment (eqn (9)) and creates an internal electric field across the interface. The induced electric field across the interface limits the charge recombination. Similarly, under UV irradiation excites TNTs (eqn (10)). The holes in the VB of TNTs migrate to the VB of the Cu_2O NPs (eqn (11)) also contribute to the charge separation. The charge separation phenomenon produces enough electrons and holes for the redox reaction, which provides enough active radicals for the photocatalytic activity, such as $^{\bullet}O_2^-$ and $^{\bullet}OH$ (eqn (12)–(15)). The active radicals continuously react with H_2O and also with each other to further form the active radicals for decomposition (eqn (16) and (17)). The $^{\bullet}OH$ radical is a strong oxidizing agent that can decompose the organic dye (eqn (18)). Moreover, the defects at the Cu_2O/TNTs HJ also play a vital role in the enhancement of photocatalytic activity by reducing the

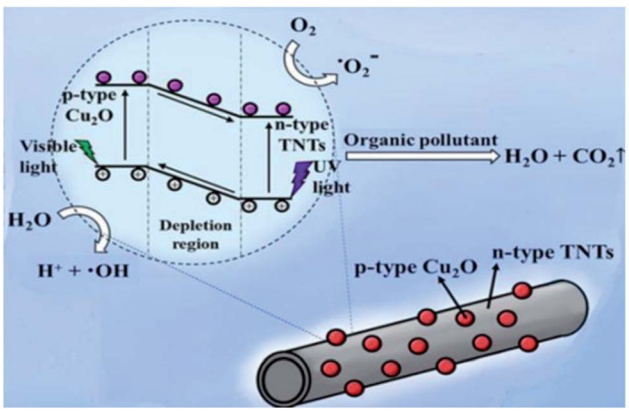

Fig. 7 Schematic diagram of the mechanism of the photocatalytic activity of the Cu_2O/TNTs heterojunction structure under sunlight irradiation.

Open Access Article. Published on 03 April 2018. Downloaded on 5/3/2026 11:28:47 AM.
This article is licensed under a Creative Commons Attribution-NonCommercial 3.0 Unported Licence.

band edge and inducing new defect levels, which serve as traps sites for the photo-induced charges and constrain the e–h recombination.[60] Furthermore, the one-dimensional TNTs act as a directional charge transport channel enhancing transport properties.

The following detailed reactions are proposed for the photocatalytic activity of Cu_2O/TNTs against MB:

$$Cu_2O \xrightarrow{\text{visible light}} Cu_2O\ (e_{CB}^- + h_{VB}^+) \quad (8)$$

$$Cu_2O\ (e_{CB}^-) + TNTs \rightarrow Cu_2O + TNTs(e_{CB}^-) \quad (9)$$

$$TNTs \xrightarrow{UV} TNTs\ (e_{CB}^- + h_{CB}^+) \quad (10)$$

$$TNTs(h_{VB}^+) + Cu_2O \rightarrow TNTs + Cu_2O(h_{CB}^+) \quad (11)$$

$$Cu_2O(e_{CB}^-) + O_2 \rightarrow Cu_2O + {}^{\bullet}O_2^- \quad (12)$$

$$TNTs(e_{CB}^-) + O_2 \rightarrow TNTs + {}^{\bullet}O_2^- \quad (13)$$

$$Cu_2O(h_{VB}^+) + H_2O \rightarrow Cu_2O + H^+ + {}^{\bullet}OH \quad (14)$$

$$TNTs(h_{VB}^+) + H_2O \rightarrow TNTs + H^+ + {}^{\bullet}OH \quad (15)$$

$${}^{\bullet}OH + H_2O \rightarrow {}^{\bullet}HO_2 + OH^- \quad (16)$$

$${}^{\bullet}HO_2 + H_2O \rightarrow H_2O_2 + {}^{\bullet}OH \quad (17)$$

$${}^{\bullet}OH + MB \rightarrow CO_2 + H_2O \quad (18)$$

Conclusions

A Cu_2O/TNTs heterojunction showing approximately double photocatalytic efficiency compared to the isolated TNTs prepared by a simple surfactant-free photoreduction method. The significant enhancement in the photocatalytic efficiency can simply be understood in terms of the narrowed band gap and improved light absorbance by the induction of additional low energy states (below the CB edge) due to the oxygen vacancies. Additionally, owing to the type II band alignment between the n-type TNTs and p-type Cu_2O NPs produce internal electric field across the interface and consequently constrain the charge recombination process across the interface. This phenomenon produces significant number of electrons and holes for the redox reaction beneficial for photocatalytic activity. Moreover, our synthetic approach of Cu_2O/TNTs junction by the photoreduction method could pave the way of removing organic dyes on an industrial scale.

Conflicts of interest

There are no conflicts to declare.

Acknowledgements

V. V. Pham would like to thank Prof. Bach Thang Phan (University of Science, VNU-HCM, Vietnam) and BK21 Plus Program for supporting this study. Y. S. Kim acknowledges support from the Priority Research Centers Program (2009-0093818), the Basic Science Research Programs (2017R1E1A1A01075350), and the Basic Research Lab Program (2014R1A4A1071686) through the National Research Foundation of Korea (NRF), funded by the Korean government.

Notes and references

1 X. Chen and S. S. Mao, *Chem. Rev.*, 2007, **107**, 2891–2959.
2 J. Schneider, M. Matsuoka, M. Takeuchi, J. Zhang, Y. Horiuchi, M. Anpo and D. W. Bahnemann, *Chem. Rev.*, 2014, **114**, 9919–9986.
3 L. Pan, S. Wang, J. Xie, L. Wang, X. Zhang and J.-J. Zou, *Nano Energy*, 2016, **28**, 296–303.
4 P. V. Viet, T. H. Huy, N. X. Sang, C. M. Thi and L. V. Hieu, *J. Mater. Sci.*, 2018, **53**, 3364–3374.
5 P. V. Viet, B. T. Phan, D. Mott, S. Maenosono, T. T. Sang, C. M. Thi and L. V. Hieu, *J. Photochem. Photobiol., A*, 2018, **352**, 106–112.
6 M. Wang, L. Sun, Z. Lin, J. Cai, K. Xie and C. Lin, *Energy Environ. Sci.*, 2013, **6**, 1211.
7 H. Wang, L. Zhang, Z. Chen, J. Hu, S. Li, Z. Wang, J. Liu and X. Wang, *Chem. Soc. Rev.*, 2014, **43**, 5234–5244.
8 M. Reza Gholipour, C. T. Dinh, F. Beland and T. O. Do, *Nanoscale*, 2015, **7**, 8187–8208.
9 J. Fu, S. Cao and J. Yu, *J. Materiomics*, 2015, **1**, 124–133.
10 G. Dai, J. Yu and G. Liu, *J. Phys. Chem. C*, 2011, **115**, 7339–7346.
11 L. Liu, W. Yang, Q. Li, S. Gao and J. K. Shang, *ACS Appl. Mater. Interfaces*, 2014, **6**, 5629–5639.
12 Y. Hou, X. Y. Li, Q. D. Zhao, X. Quan and G. H. Chen, *Appl. Phys. Lett.*, 2009, **95**, 093108.
13 T. Han, D. Zhou and H. Wang, *Powder Technol.*, 2016, **301**, 959–965.
14 Z. Wang, Y. Liu, D. J. Martin, W. Wang, J. Tang and W. Huang, *Phys. Chem. Chem. Phys.*, 2013, **15**, 14956–14960.
15 W.-Y. Cheng, T.-H. Yu, K.-J. Chao and S.-Y. Lu, *ChemCatChem*, 2014, **6**, 293–300.
16 S. Wang, X. Zhang, L. Pan, F.-M. Zhao, J.-J. Zou, T. Zhang and L. Wang, *Appl. Catal., B*, 2015, **164**, 234–240.
17 L. Pan, J.-J. Zou, T. Zhang, S. Wang, Z. Li, L. Wang and X. Zhang, *J. Phys. Chem. C*, 2013, **118**, 16335–16343.
18 Y. Hou, X. Li, X. Zou, X. Quan and G. Chen, *Environ. Sci. Technol.*, 2009, **43**, 858–863.
19 L. Xiang, J. Ya, F. Hu, L. Li and Z. Liu, *Appl. Phys. A: Mater. Sci. Process.*, 2017, **123**(3), 60.
20 S. Zhang, C. Liu, X. Liu, H. Zhang, P. Liu, S. Zhang, F. Peng and H. Zhao, *Appl. Microbiol. Biotechnol.*, 2012, **96**, 1201–1207.
21 H. Li, L. Cao, W. Liu, G. Su and B. Dong, *Ceram. Int.*, 2012, **38**, 5791–5797.

 This journal is © The Royal Society of Chemistry 2018

Open Access Article. Published on 03 April 2018. Downloaded on 5/3/2026 11:28:47 AM.
This article is licensed under a Creative Commons Attribution-NonCommercial 3.0 Unported Licence.

22 G. K. Mor, O. K. Varghese, M. Paulose, N. Mukherjee and C. A. Grimes, *J. Mater. Res.*, 2011, **18**, 2588–2593.
23 H. P. Quiroz and A. Dussan, *J. Appl. Phys.*, 2016, **120**, 051703.
24 Y. Zhou, C. Y. Wang, Y. R. Zhu and Z. Y. Chen, *Chem. Mater.*, 1999, **11**, 2310–2312.
25 M. K. Abyaneh, D. Paramanik, S. Varma, S. W. Gosavi and S. K. Kulkarni, *J. Phys. D: Appl. Phys.*, 2007, **40**, 3771–3779.
26 M. K. I. Senevirathna, P. K. D. D. P. Pitigala and K. Tennakone, *J. Photochem. Photobiol., A*, 2005, **171**, 257–259.
27 K. Dong, J. He, J. Liu, F. Li, L. Yu, Y. Zhang, X. Zhou and H. Ma, *J. Mater. Sci.*, 2017, **52**, 6754–6766.
28 X. An, H. Liu, J. Qu, S. J. A. Moniz and J. Tang, *New J. Chem.*, 2015, **39**, 314–320.
29 P. V. Viet, B. T. Phan, L. V. Hieu and C. M. Thi, *J. Nanosci. Nanotechnol.*, 2015, **15**, 5202–5206.
30 H. Wang, Z. Wu, W. Zhao and B. Guan, *Chemosphere*, 2007, **66**, 185–190.
31 H. S. Son, S. J. Lee, I. H. Cho and K. D. Zoh, *Chemosphere*, 2004, **57**, 309–317.
32 Y. Li, B. Wang, S. Liu, X. Duan and Z. Hu, *Appl. Surf. Sci.*, 2015, **324**, 736–744.
33 T. Ohsaka, F. Izumi and Y. Fujiki, *J. Raman Spectrosc.*, 1978, **7**, 321–324.
34 D. Georgescu, L. Baia, O. Ersen, M. Baia and S. Simon, *J. Raman Spectrosc.*, 2012, **43**, 876–883.
35 S. P. S. Porto, P. A. Fleury and T. C. Damen, *Phys. Rev.*, 1967, **154**, 522–526.
36 Y. Liu, F. Ren, S. Shen, Y. Fu, C. Chen, C. Liu, Z. Xing, D. Liu, X. Xiao, W. Wu, X. Zheng, Y. Liu and C. Jiang, *Appl. Phys. Lett.*, 2015, **106**, 123901.
37 L. Qian, Z.-L. Du, S.-Y. Yang and Z.-S. Jin, *J. Mol. Struct.*, 2005, **749**, 103–107.
38 J. E. Moulder, W. F. Stickle, P. E. Sobol and K. D. Bomben, in *Handbook of X-Ray Photoelectron Spectroscopy*, ed. J. Chastain and R. C. Eing Jr, Physical Electronics Inc., Minnesota, USA, 1995, vol. 93.
39 B. Xin, D. Ding, Y. Gao, X. Jin, H. Fu and P. Wang, *Appl. Surf. Sci.*, 2009, **255**, 5896–5901.
40 B. Bharti, S. Kumar, H. N. Lee and R. Kumar, *Sci. Rep.*, 2016, **6**, 32355.
41 S. Sakthivel, M. C. Hidalgo, D. W. Bahnemann, S. U. Geissen, V. Murugesan and A. Vogelpohl, *Appl. Catal., B*, 2006, **63**, 31–40.
42 Y.-h. Xu, D.-h. Liang, M.-l. Liu and D.-z. Liu, *Mater. Res. Bull.*, 2008, **43**, 3474–3482.
43 D. Wang, X. Pan, G. Wang and Z. Yi, *RSC Adv.*, 2015, **5**, 22038–22043.
44 Z. Luo, H. Jiang, D. Li, L. Hu, W. Geng, P. Wei and P. Ouyang, *RSC Adv.*, 2014, **4**, 17797.
45 M. Arai, S. Nishiyama, S. Tsuruya and M. Masai, *J. Chem. Soc., Faraday Trans.*, 1996, **92**, 2631.
46 J. Yu and J. Ran, *Energy Environ. Sci.*, 2011, **4**, 1364.
47 M. Liu, X. Qiu, K. Hashimoto and M. Miyauchi, *J. Mater. Chem. A*, 2014, **2**, 13571–13579.
48 T. Morikawa, Y. Irokawa and T. Ohwaki, *Appl. Catal., A*, 2006, **314**, 123–127.
49 A. Murphy, *Sol. Energy Mater. Sol. Cells*, 2007, **91**, 1326–1337.
50 H. Yin, X. Wang, L. Wang, Q. N. and H. Zhao, *J. Alloys Compd.*, 2015, **640**, 68–74.
51 J. Li, X. Xu, X. Liu, C. Yu, D. Yan, Z. Sun and L. Pan, *J. Alloys Compd.*, 2016, **679**, 454–462.
52 X. Chen, L. Liu, P. Y. Yu and S. S. Mao, *Science*, 2011, **331**, 746–750.
53 Y. Lei, L. D. Zhang, G. W. Meng, G. H. Li, X. Y. Zhang, C. H. Liang, W. Chen and S. X. Wang, *Appl. Phys. Lett.*, 2001, **78**, 1125–1127.
54 Y. Du, W. L. Cai, C. M. Mo, J. Chen, L. D. Zhang and X. G. Zhu, *Appl. Phys. Lett.*, 1999, **74**, 2951–2953.
55 W. Chen, H. Tang, C. Shi, J. Deng, J. Shi, Y. Zhou, S. Xia, Y. Wang and S. Yin, *Appl. Phys. Lett.*, 1995, **67**, 317–319.
56 A. Aronne, M. Fantauzzi, C. Imparato, D. Atzei, L. De Stefano, G. D'Errico, F. Sannino, I. Rea, D. Pirozzi, B. Elsener, P. Pernice and A. Rossi, *RSC Adv.*, 2017, **7**, 2373–2381.
57 L.-B. Xiong, J.-L. Li, B. Yang and Y. Yu, *J. Nanomater.*, 2012, **2012**, 1–13.
58 L. Z. Liu, J. Q. Xu, X. L. Wu, T. H. Li, J. C. Shen and P. K. Chu, *Appl. Phys. Lett.*, 2013, **102**, 031916.
59 J. Liqiang, Q. Yichun, W. Baiqi, L. Shudan, J. Baojiang, Y. Libin, F. Wei, F. Honggang and S. Jiazhong, *Sol. Energy Mater. Sol. Cells*, 2006, **90**, 1773–1787.
60 J. Liu, J. Ke, D. Li, H. Sun, P. Liang, X. Duan, W. Tian, M. O. Tade, S. Liu and S. Wang, *ACS Appl. Mater. Interfaces*, 2017, **9**, 11678–11688.